Computational prediction of nanostructured alloys with enhanced thermoelectric properties

Jeff W. Doak, Shiqiang Hao, Scott Kirklin, and Christopher Wolverton

Phys. Rev. Materials **3**, 105404 — Published 8 October 2019

DOI: 10.1103/PhysRevMaterials.3.105404

Computational prediction of nanostructured alloys with enhanced thermoelectric properties

Jeff W. Doak, Shiqiang Hao, Scott Kirklin, and Christopher Wolverton
Department of Materials Science and Engineering,
Northwestern University, Evanston, Illinois, USA 60208

The Materials Genome Initiative calls for a dramatic increase in the rate of materials discovery and development. High-throughput (HT) calculations can advance this goal by efficiently screening a large search space for candidate materials to study in more depth. Thermoelectric materials (TEs) are prime candidates for such HT calculations: the properties required to achieve good performance are known, but systematic ways of improving these properties are scarce. Furthermore, known HT methods for TEs only address bulk crystals—screening realistic multicomponent alloys for their TE properties has yet to be accomplished. In this work, we use a density functional theory driven HT screening-and-sorting procedure to search for new multicomponent bulk-nanostructured thermoelectric materials. We make maximum use of minimal calculations to obtain eight descriptors of the thermodynamics and TE performance of 5-element semiconductor alloy systems from combinations of ternary additions in binary compounds. We use these descriptors to reduce a search space of 29,700 5-element systems to a set of 130 candidates. We screen these candidates using TE descriptors to identify several existing high-performance thermoelectrics as well as promising new material systems awaiting further experimental verification.

I. INTRODUCTION

First-principles calculations of materials have advanced to the point where high-throughput calculations can be performed on a wide variety of systems to calculate a diverse variety of properties.[1–7] Such high-throughput calculations form a cornerstone of the Materials Genome Initiative,[8] which has a goal of accelerating the rate of materials discovery and decreasing the time from materials discovery to product deployment. Thermoelectric devices are one materials application where first-principles calculations can provide considerable support, and there have been several high-throughput efforts to identify new promising compounds with favorable thermoelectric properties.[9–16] However, the best thermoelectric *materials* are multicomponent semiconductor alloys that would never be identified in these studies.

Thermoelectric materials generate electricity from waste heat and have the potential to improve the efficiency of heat-generating power sources such as power plants and car engines. In order to make thermoelectric devices economically viable, the energy conversion efficiency of thermoelectric materials, characterized by the figure of merit ZT ($= \frac{S^2\sigma}{\kappa_e+\kappa_l}T$), need to be increased from typical values around 1 to 4.[17] Recently, thermoelectric materials with ZT above 2 have been synthesized using a variety of techniques to reduce the lattice thermal conductivity (κ_l) while simultaneously increasing the electrical conductivity (σ) and Seebeck coefficient (S).[18]

These techniques to increase ZT include (i) precipitating (semi)coherent nanostructures out of the bulk, reducing κ_l;[19–30] (ii) finding nanostructures that have a valence band closely aligned with that of the bulk matrix phase, increasing the carrier mobility across the nanostructures and thereby σ;[23,26,29] (iii) adding alloying elements to the bulk which shift the energy level of a second valence band closer to the valence band maximum (VBM) of the matrix phase, increasing the band degeneracy, and through it S;[29,31] and (iv) refining the grain size through spark-plasma sintering (SPS), scattering long-wavelength phonons and reducing κ_l.[27,29,32–34] Of these methods of improving ZT, (i), (ii), and (iii) involve altering the chemistry of the material to achieve the desired properties.[35]

Exploration of this variation in chemistry has largely been performed through an Edisonian process of trial and error. In this work, we use first-principles calculations to systematically explore the chemical space available to alloys of the IV–VI compounds. We calculate descriptors related to the thermodynamics and desired thermoelectric property changes for 5-element alloys with constituent elements chosen from a set of ten cations and three anions in AX rocksalt compounds (a total of 29,700 systems), screen these systems based on their thermodynamics, and sort the screened systems based on their thermoelectric performance. We identify materials systems which have already received attention as promising thermoelectric alloys as well as several new systems of interest for further experimental study.

II. RESULTS

A computational search for new *alloy* systems with improved thermoelectric properties must consider two aspects of the problem: identifying systems which can be prepared in the lab and identifying systems with enhanced thermoelectric properties. To address the first aspect of this problem, identifying alloy systems which will form desired nanostructures (which will give enhanced thermoelectric properties), we must identify descriptors related to the thermodynamics required to achieve the desired nanostructures. To address the second aspect of this problem, identifying alloy systems which can take advantage of the ZT-enhancing techniques (i)–(iii) described above, we must identify descriptors related to the properties being enhanced which can be calculated readily within density functional theory (DFT). Once we have these descriptors, we can screen out systems with unfavorable thermodynamics and electronic structures before sorting the remaining systems and identifying the most-promising candidates. Figure 1 shows the desired nanostructure, composition space we will search, and our screening work flow which will be described in the next sections.

A. Descriptors/Search Strategy

The nanostructure shown schematically in Fig. 1(a) consists of a rocksalt matrix phase AX alloyed with an element C, in which rocksalt nanostructures BX or AY (for brevity we will use BX in the following descriptions) alloyed with an element D are embedded. This type of nanostructure can be created through phase separation within the bulk of an alloy thermoelectric[19] and has been shown to enhance ZT of thermoelectric systems by reducing the lattice thermal conductivity.[19–30] In order for this type of phase-separated nanostructure to form, there must be a (positive) thermodynamic driving force for the nanostructure to phase separate from the matrix. In addition, for C to alloy the matrix and not the nanostructure, C must be soluble in the matrix and C must have a thermodynamic preference for the matrix over the nanostructure. The opposite considerations apply for the element D to alloy the nanostructure and

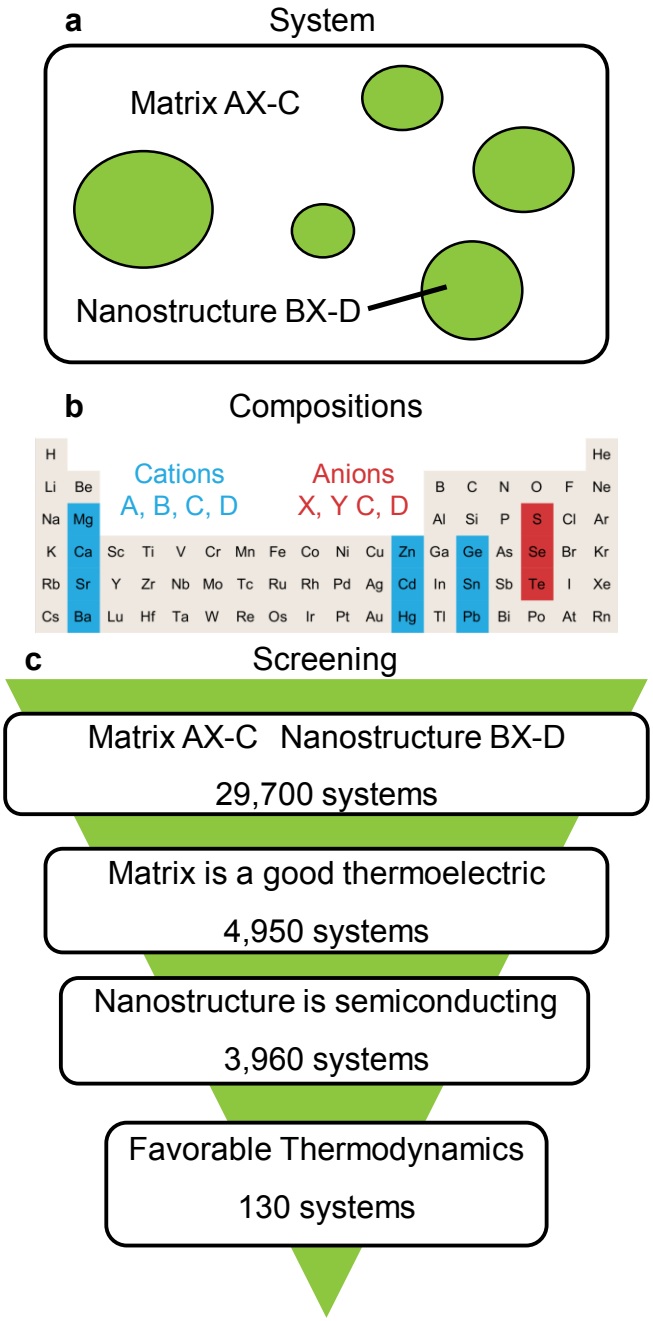

FIG. 1. Nanostructured thermoelectric alloy design and high-throughput work flow. **a** Schematic diagram of thermoelectric alloy consisting of a matrix compound (AX), a nanostructured compound (BX), matrix-alloying element (C), and nanostructure-alloying element (D). **b** Set of cations (blue) and anions (red) defining our search space. **c** Flowchart for screening 29,700 systems down to 130 systems for sorting.

not the matrix—D must be soluble in the nanostructure and have a thermodynamic preference for the nanostructure over the matrix. Elements A and B are cations taken from the list of +2 elements shown in blue in Fig. 1(b). Elements X and Y are anions taken from the list of −2 elements shown in red in Fig. 1(b). Elements C and D can be cations or anions and are taken from the combined list. We require the matrix phase to be rocksalt in its equilibrium structure, but the nanostructures can form rocksalt as a metastable, constrained phase.[26] These thermodynamic considerations lead us to identify the following descriptors, which can be obtained directly from DFT total energies as described in Sec. IV:

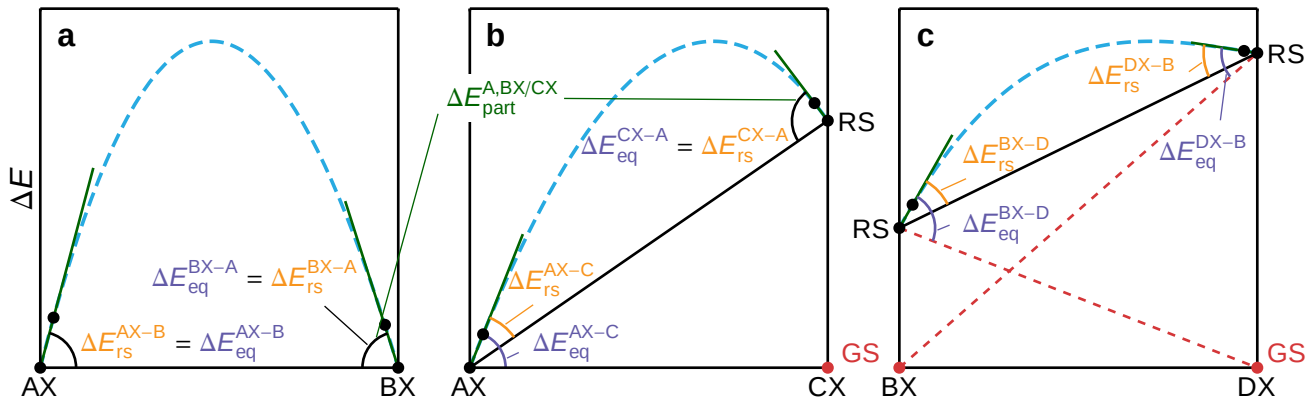

FIG. 2. Thermodynamic properties used to screen and sort alloy systems. Points correspond to DFT formation energies relative to the end-member compounds. Solid lines indicate equilibrium between two rocksalt phases. Dashed red lines indicate equilibrium between a rocksalt and non-rocksalt phase. Arcs indicate the difference in slope between two lines on a plot. Thermodynamic descriptors are shown for three cases. (**a**) matrix AX and nanostructure BX are rocksalt in their groundstates. (**b**) matrix AX is rocksalt and nanostructure CX is metastable in rocksalt or matrix alloy C does not form rocksalt with X. (**c**) nanostructure BX is metastable in rocksalt and nanostructure alloy D does not form rocksalt with X. The driving force for forming nanostructures $\Delta E_{\text{rs}}^{\text{AX-B}}$ is the difference in slope between a dilute amount of B in AX and equilibrium between AX and BX, both in the rocksalt phase. The driving force for precipitation of CX from AX $\Delta E_{\text{eq}}^{\text{AX-C}}$ is the difference in slope between a dilute amount of C in AX and equilibrium between AX and CX, AX in rocksalt and CX in its equilibrium structure. The partitioning energy of A between BX and CX is given by the difference in $\Delta E_{\text{eq}}^{\text{BX-A}}$ and $\Delta E_{\text{eq}}^{\text{CX-A}}$. We define the formation energy of 0.01 eV about the hull as metastable phase.

1. a positive thermodynamic driving force for the formation of BX nanostructures from the AX matrix $\Delta E_{\text{rs}}^{\text{AX-B}} > 0$,
2. a high solubility of C in AX (i.e. low driving force for precipitation of CX or AC $\Delta E_{\text{eq}}^{\text{AX-C}}$),
3. a similarly high solubility of D in BX,
4. an energetic preference for C to go into AX over BX (partitioning of C to AX over BX) ($\Delta E_{\text{part}}^{\text{C,AX/BX}} < 0$), and
5. partitioning of D to BX over AX ($\Delta E_{\text{part}}^{\text{D,BX/AX}} < 0$).

These thermodynamic descriptors are shown schematically in Fig. 2.

The desired ZT-enhancing techniques are to:

1. form coherent nanostructures to scatter phonons and hence lower thermal conductivity,
2. alloy the matrix and nanostructure to minimize the valence band offset between the matrix and nanostructure, hence keeping carrier mobility high, and
3. alloy the matrix to bring the valence bands at L and Σ in the rocksalt Brillouin Zone (BZ) closer in energy, hence increasing the Seebeck coefficient.

The descriptors corresponding to the above techniques (with the number of the descriptor corresponding to the number of the ZT-enhancing technique) are:

1a. the lattice mismatch between AX and BX/AY $a_{\text{mis}}^{\text{AX/BX}}$,

1b. the thermodynamic driving force for the formation of nanostructures $\Delta E_{\text{rs}}^{\text{AX-B}}$,

2. the valence band alignment (assuming p-type semiconductors) between the matrix and nanostructure $|\Delta\varepsilon_{\text{VBM}}^{\text{BX-D/AX-C}}|$, and
3. the energy difference between the valence band (VB) at L and Σ, $\Delta\varepsilon_{\text{V,L}-\Sigma}^{\text{AX-C}}$.

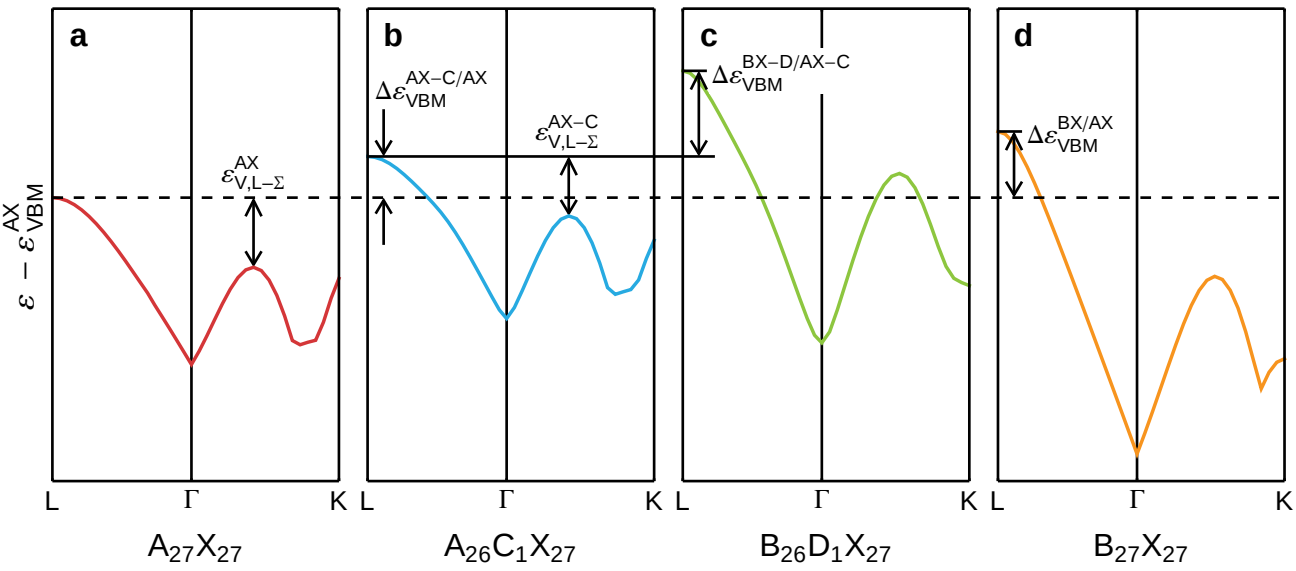

FIG. 3. Electronic-structure properties used to sort alloy systems. The valence band structures of 54-atom supercells of rocksalt systems are shown schematically for **a** $A_{27}X_{27}$, **b** $A_{26}C_1X_{27}$, **c** $B_{26}D_1X_{27}$, and **d** $B_{27}X_{27}$, all relative to the VBM of $A_{27}X_{27}$. The valence band structure of **b** is aligned to the valence band structure of **a** through the electrostatic potentials of the two calculations. The valence band structures of **c** and **d** are aligned similarly. The valence band structures of **a** and **d** are aligned to the universal hydrogen +/- transition level. By combining these three band alignments, we can directly compare the valence band energies of **b** and **c**, $|\Delta\varepsilon^{\text{BX-D/AX-C}}_{\text{VBM}}|$. By comparing the difference in valence band energies at L and along Σ in **b** and **a** ($\varepsilon^{\text{AX-C}}_{\text{V,L}-\Sigma}$ and $\varepsilon^{\text{AX}}_{\text{V,L}-\Sigma}$, respectively) we obtain $\Delta\varepsilon^{\text{AX-C}}_{\text{V,L}-\Sigma}$. Note that Σ is along the high-symmetry Γ-K direction.

These electronic structure descriptors are shown schematically in Fig. 3.

All of these descriptors can be obtained from DFT calculations of supercells of a rocksalt compound with a single cation, anion, or hydrogen impurity. There are a total of 360 ways of choosing AX-C from our list of ten cations and three anions (including the pure AX compound where C=A or C=X), and so there are 360 calculations required to obtain thermodynamic and electronic structure data for each of these systems. In addition, 60 calculations of $+/-$ charged interstitial hydrogen defects in the 30 AX compounds are required to obtain the universal band alignment of the pure rocksalt phases.[36] (See Sec. IV for details of our computational methodology.) We combine these 420 calculations to obtain descriptors for the 29,700 combinations of AX, BX/AY, C, and D.

B. Screening

To search our set of 29,700 candidate alloy systems for promising thermoelectric alloys, we first screen out the systems which have unfavorable descriptors using the screens illustrated in Fig. 1(c). First, we remove systems where the AX matrix phase is not a good bulk thermoelectric material in its own right (accounting for the favorable values of σ, S, and κ_e which we have not calculated directly). We take as 'good bulk thermoelectrics' the compounds PbTe, PbSe, PbS, SnTe, and GeTe. These are the IV-VI compounds which form in the rocksalt structure at operating temperatures. This first screen reduces our search space from 29,700 systems to 4,950 systems. We next screen out systems where the (metastable) BX or AY rocksalt nanostructure is a metal within DFT. This is the case for ZnTe, CdTe, HgS, HgSe, and HgTe. Removing systems with these compounds as nanostructures leaves us with 3,960 systems in our search space. Our third and final screen removes systems with thermodynamics which are unfavorable for the formation of the nanostructure of Fig. 1(a). The conditions for favorable thermodynamics are:

1. a positive driving force for forming a BX nanostructure $\Delta E^{\text{AX-B}}_{\text{rs}} > 0$,
2. a low driving force for precipitation of the alloying element C from the matrix AX $0 < \Delta E^{\text{AX-C}}_{\text{eq}} < 0.2$ eV/solute,
3. a low driving force for precipitation of the alloying element D from the nanostructure BX $0 < \Delta E^{\text{BX-D}}_{\text{eq}} < 0.2$ eV/solute,

4. partitioning of C to AX over BX $\Delta E_{\text{part}}^{\text{C,AX/BX}} < 0$, and

5. partitioning of D to BX over AX $\Delta E_{\text{part}}^{\text{D,BX/AX}} < 0$.

In 2. and 3. we choose an upper bound of 0.2 eV/solute for the driving force which corresponds to a lower limit of 2% solubility for the alloying elements C and D at 600 K. These thermodynamic screens leave us with 130 systems for potential thermoelectric alloys. This 130 5-element screened search space is still much too large to be of practical use. In the following section we sort this space using thermodynamic and electronic structure descriptors to identify the most promising of these 130 candidate systems.

C. Sorting

We use two techniques to sort the remaining 130 systems based on their electronic-structure descriptors: Pareto set identification[37] and rank aggregation[38] (see Sec. IV). Pareto analysis provides a method to obtain all of the systems which optimize a multi-dimensional objective function. Pareto analysis has been applied to several materials design and selection problems, including some of the first high-throughput DFT calculation analyses.[1,39,40] In this work the multi-dimensional objective function is the combination of lattice mismatch, driving force for nanostructures, valence band alignment, and valence band shifting. In addition to Pareto analysis, we use rank aggregation to combine the lists of systems sorted by each of the four descriptors above into one sorted master list which incorporates each of the individual rankings.

The results of our screening and sorting are shown in Fig. 4 through cross-plots of the six possible pairs of the four sorting descriptors above. In each panel of Fig. 4, the full set of 29,700 systems are shown as open green circles, the set of 130 screened systems are shown as closed blue circles, the Pareto front for each of the 2-D cross-plots are shown as orange circles connected by lines, and the top-10 rank-aggregated systems are shown as red circles. The axes of each panel are chosen so that more optimal systems are found closer to the lower-left corner of each plot. The first panel of the plot, $\Delta E_{\text{rs}}^{\text{AX-B}}$ vs. $a_{\text{mis}}^{\text{AX/BX}}$ shows a clear functional relationship: $\Delta E_{\text{rs}}^{\text{AX-B}} \propto (a_{\text{mis}}^{AX/BX})^2$. This relationship has been noted previously for the (IV,IV)–VI and IV–(VI,VI) alloys,[41] and the dashed line in this panel shows a fit to all of the data. Because $\Delta E_{\text{rs}}^{\text{AX-B}}$ vs. $a_{\text{mis}}^{\text{AX/BX}}$ has a strong functional relationship and because this relationship opposes our design goals (minimize $a_{\text{mis}}^{\text{AX/BX}}$ while maximizing $\Delta E_{\text{rs}}^{\text{AX-B}}$), this cross-plot seems to be the most limiting and therefore important. The systems which deviate most from this trend of $\Delta E_{\text{rs}}^{\text{AX-B}} \propto (a_{\text{mis}}^{AX/BX})^2$ are SnTe/CaTe, SnTe/SrTe, and GeTe/CaTe. These systems are denoted on all cross-plots of Fig. 4. In addition, two well-studied systems, PbTe/PbS[19] and PbTe/SrTe,[23,27] are also shown on each of the cross-plots. These systems also tend to have good VBM alignment but lie towards the higher range of the VB shift $\Delta\varepsilon_{\text{V,L}-\Sigma}^{\text{AX-C}}$.

There are 31 systems which lie on the 4-D Pareto front of these descriptors, which are listed in Table II. Included among these systems on the Pareto front are eight already engineered thermoelectric materials including PbTe–SrTe,[23,27] PbTe–PbS,[19,32] and PbSe–CdSe.[29] The experimental systems have been nanostructured, but not simultaneously nanostructured and alloyed, so further enhancement in ZT should be feasible for these systems. In addition to Pareto analysis we use rank aggregation to combine the lists of systems sorted by each of the four descriptors above into one sorted master list which incorporates each of the individual rankings. The top-10 ranked systems shown in red in Fig. 4 are listed in Table I. Seven of the top-10 ranked systems lie on the Pareto front. From our list of top-10 systems and systems on the Pareto front, we identify several systems that have not been investigated experimentally, but which show promise as potential thermoelectric materials. SnTe/CaTe has the lowest lattice mismatch of the screened systems and both SnTe-Pb/CaTe-Se and SnTe-Pb/CaTe-Sr are in the top-10 list. Another promising candidate is PbSe-Sr/SnSe-Ge, which does not deviate from the $\Delta E_{\text{rs}}^{\text{AX-B}} \propto (a_{\text{mis}}^{\text{AX/BX}})^2$ curve, but lies on the Pareto front for $|\Delta\varepsilon_{\text{VBM}}^{\text{AX-C/BX-D}}|$ vs. $a_{\text{mis}}^{\text{AX/BX}}$.

III. CONCLUSIONS

In this work we used high-throughput DFT-based descriptors to evaluate semiconductor alloy systems for their thermoelectric performance. These descriptors were based on experimental design heuristics for how alloying affects ZT. This approach avoids problems with calculating ZT using DFT: underestimated band gaps give poor S values, the unrealistic constant relaxation time approximation is required to obtain any σ values, and ZT can only be calculated for pure compounds. We searched through an extremely large combinatorial space, screening out over 29,000 potential thermoelectric material systems as having unfavorable thermodynamics for synthesis. We sorted the remaining 130 candidate systems based on their electronic-structure properties, found several existing thermoelectric

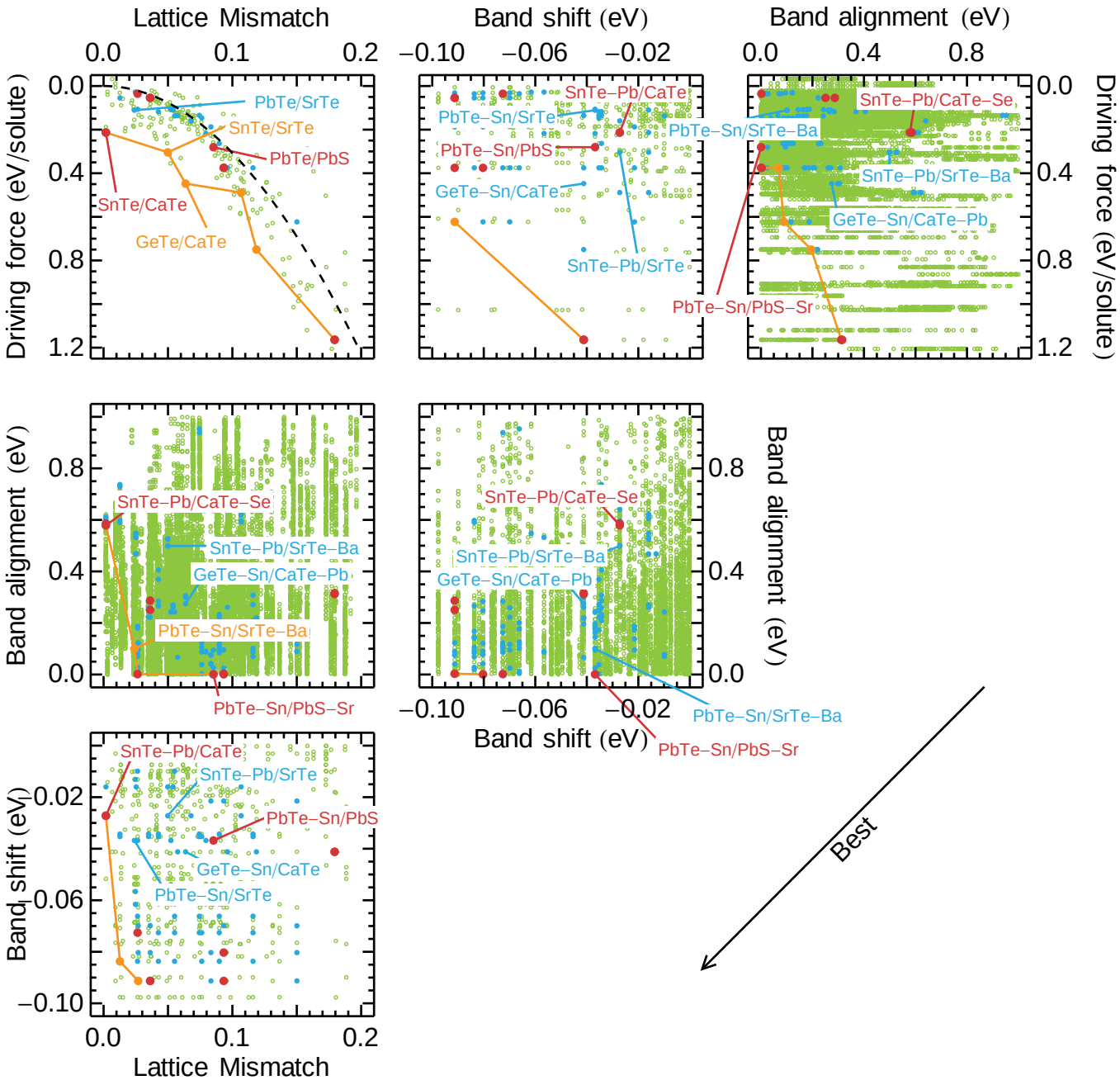

FIG. 4. High-throughput screening and sorting. Data for each set of AX, BX, C, and D elements relevant to thermoelectric performance are projected onto pairs of axes of the four-dimensional descriptor space. Data for all 29,700 unscreened systems are shown as open green circles. Data for the 130 screened systems are shown as closed blue circles. Pareto fronts for each two-dimensional subset of screened data are shown as connected orange circles in each plot. Top-10 ranked systems of the screened data are shown as closed red circles.

alloys with our analysis, and identified new promising thermoelectric material systems, including SnTe-Pb/CaTe-Se, SnTe-Pb/SrTe-Ba, and GeTe-Sn/CaTe-Pb. These materials systems are ideal candidates for future experimental investigation and validation. As can be seen, we have considered isoelectronic dopants to tune the band alignment and degeneracy between matrix and host materials. However, the charged dopants are becoming more and more important, since the charged dopants are on the one hand adjusting the carrier concentration and on the other hand decreasing lattice thermal conductivities. So, it will be very interesting to examine the charged alloying materials for enhanced thermoelectric systems in the future.

TABLE I. Top-10 rank-aggregated systems. These systems simultaneously (i) maximize the driving force for nanostructures $\Delta E_{\mathrm{rs}}^{\mathrm{AX\text{-}B}}$, (ii) minimize the lattice mismatch $a_{\mathrm{mis}}^{\mathrm{AX/BX}}$, (iii) minimize the energy difference between VB at L and Σ, $\Delta\varepsilon_{\mathrm{V,L-}\Sigma}^{\mathrm{AX\text{-}C}}$, and (iv) minimize the valence band offset $|\Delta\varepsilon_{\mathrm{VBM}}^{\mathrm{BX\text{-}D/AX\text{-}C}}|$ between matrix and nanostructure. The possible formation of ternary phases is not considered in the driving force calculations.

Matrix AX	Nanostructure BX/AY	Mat-Alloy C	Nano-Alloy D	Exp. System	ZT @ T (K)	Ref.
PbS	PbTe	Ba	Sn	$PbS_{0.97}Te_{0.03}$–0.1% $PbCl_2$	0.8 @ 900	25
GeTe	BaTe	Sn	Se	-	-	-
SnTe	CaTe	Pb	Se	-	-	-
SnTe	CaTe	Pb	Sr	-	-	-
PbTe	PbS	Sn	Sr	$Pb_{1-x}Sn_xTe$–PbS	1.5 @ 642	19
-	-	-	-	$PbTe_{0.7}S_{0.3}$–2.5% K	2.2 @ 923	32
PbS	PbSe	Ba	Te	-	-	-
PbS	PbSe	Ba	Sn	-	-	-
PbS	PbTe	Sr	Sn	$PbS_{0.97}Te_{0.03}$–0.1% $PbCl_2$	0.8 @ 900	25
PbSe	SnSe	Sr	Ge	-	-	-
GeTe	BaTe	Sn	Sr	-	-	-

IV. METHODS

A. Computational Methodology

DFT[42,43] calculations were performed with the Vienna *Ab initio* Simulation Package (VASP)[44] using the exchange-correlation functional of Perdew, Burke, and Ernzerhoff (PBE)[45] and projector-augmented wave (PAW)[46] potentials. Total energies of 54-atom rocksalt supercells (perfect crystals and crystals containing one substitutional defect) were calculated using 520 eV energy cutoffs and $5 \times 5 \times 5$ Γ-centered k-point meshes. Further calculation details, including automation methods, can be found in Ref.

DFT-calculated properties were analyzed using Pareto analysis and rank aggregation. Pareto analysis determines the set of 'best compromises' for a multi-objective function optimization problem—the Pareto front.37 Each of the points on the Pareto front is not strictly worse than any other point in the dataset with regards to the multi-dimensional objective function. Rank aggregation reduces a multi-objective function optimization problem down to a single-objective-function optimization problem by combining multiple ranked lists (objective functions) into one ranked list which tries to incorporate the rank of each entry in the input lists. We perform rank aggregation using a weighted Spearman's footrule measure47 as our objective function, which is optimized using cross-entropy Monte Carlo with the RankAggreg R package.38

B. Calculation of Descriptors

The descriptors presented in Sec. II A are obtained from our 54-atom DFT supercell calculations using (a) the DFT volume of the rocksalt compounds, (b) the DFT total energies, (c) the DFT valence band structures along the path L—Γ—K in the rocksalt BZ, (d) the VBM relative to the hydrogen transition level $\varepsilon_{\mathrm{H}}^{+/-}$, and (e) the average electrostatic potential difference between AX-C and AX calculations $\Delta V_{\mathrm{PA}}^{\mathrm{AX\text{-}C}}$.

1. Lattice mismatch

The lattice misfit, or lattice parameter mismatch, between an AX matrix and a BX nanostructure, is determined from the relaxed DFT volumes of the supercells of the pure matrix and nanostructure phases. The lattice parameter of each compound, a, is found from the total volume of the 54-atom supercell, V, using $a = \sqrt[3]{\frac{4}{27}V}$. The lattice misfit between the matrix and nanostructure is then

$$a_{\mathrm{mis}}^{\mathrm{AX/BX}} = \frac{|a_{\mathrm{AX}} - a_{\mathrm{BX}}|}{a_{\mathrm{AX}}}. \tag{1}$$

2. Thermodynamic descriptors

The thermodynamic driving force for precipitation of a rocksalt phase BX from a rocksalt matrix AX can be estimated from the dilute-limit energy of B in AX (and similarly for anion-mixing systems AX and AY), constrained to the rocksalt structure, calculated using

$$\Delta E_{\mathrm{rs}}^{\mathrm{AX\text{-}B}} = E_{\mathrm{tot}}^{\mathrm{AX\text{-}B}} - \frac{26}{27}E_{\mathrm{tot}}^{\mathrm{AX}} - \frac{1}{27}E_{\mathrm{tot}}^{\mathrm{BX}}, \tag{2}$$

where $E_{\mathrm{tot}}^{\mathrm{AX\text{-}B}}$, $E_{\mathrm{tot}}^{\mathrm{AX}}$, and $E_{\mathrm{tot}}^{\mathrm{BX}}$ are the DFT total energies of the 54-atom rocksalt supercells of $A_{26}B_1X_{27}$, $A_{27}X_{27}$, and $B_{27}X_{27}$, respectively.

The thermodynamic driving force for the precipitation of the equilibrium phase CX from a rocksalt matrix AX can be estimated by the dilute-limit energy of C in AX relative to the equilibrium compound CX, calculated using

$$\Delta E_{\mathrm{eq}}^{\mathrm{AX\text{-}C}} = E_{\mathrm{tot}}^{\mathrm{AX\text{-}C}} - E_{\mathrm{tot}}^{\mathrm{AX}} - \mu_{\mathrm{C}} + \mu_{\mathrm{A}}. \tag{3}$$

The chemical potentials μ_{A} and μ_{C} are found by solving

$$E_{\mathrm{rs}}^{\mathrm{AX}} = \frac{1}{2}\mu_{\mathrm{A}} + \frac{1}{2}\mu_{\mathrm{X}}, \tag{4}$$

$$E_{\mathrm{eq}}^{\mathrm{CX}} = \frac{1}{2}\mu_{\mathrm{C}} + \frac{1}{2}\mu_{\mathrm{X}}, \tag{5}$$

where $E_{\mathrm{eq}}^{\mathrm{CX}}$ is the DFT total energy of the equilibrium phase CX obtained from the Open Quantum Materials Database (OQMD).3 and 7

The partitioning energy of a solute C between a matrix AX and nanostructure BX is obtained from the DFT total energies using

$$\Delta E_{\mathrm{part}}^{\mathrm{C,AX/BX}} = \left(E_{\mathrm{tot}}^{\mathrm{AX\text{-}C}} - \frac{26}{27}E_{\mathrm{tot}}^{\mathrm{AX}}\right) - \left(E_{\mathrm{tot}}^{\mathrm{BX\text{-}C}} - \frac{26}{27}E_{\mathrm{tot}}^{\mathrm{BX}}\right), \tag{6}$$

$$\Delta E_{\mathrm{part}}^{\mathrm{C,AX/BX}} = \left(E_{\mathrm{tot}}^{\mathrm{AX\text{-}C}} - E_{\mathrm{tot}}^{\mathrm{AX}}\right) - \left(E_{\mathrm{tot}}^{\mathrm{BX\text{-}C}} - E_{\mathrm{tot}}^{\mathrm{BX}}\right), \tag{7}$$

if C is a cation or anion, respectively. Similarly, the partitioning of an element C between a matrix AX and nanostructure AY are given by Eqs. (7) and (6), respectively.

3. Electronic-structure descriptors

The change in the valence band (VB) energies of a compound AX at L and Σ upon alloying with an element C is given by

$$\Delta\varepsilon_{\mathrm{V,L-\Sigma}}^{\mathrm{AX\text{-}C}} = \left(\varepsilon_{\mathrm{V,L}}^{\mathrm{AX\text{-}C}} - \varepsilon_{\mathrm{V,\Sigma}}^{\mathrm{AX\text{-}C}}\right) - \left(\varepsilon_{\mathrm{V,L}}^{\mathrm{AX}} - \varepsilon_{\mathrm{V,\Sigma}}^{\mathrm{AX}}\right), \tag{8}$$

where $\varepsilon_{\mathrm{V},i}^{\mathrm{AX}}$ and $\varepsilon_{\mathrm{V},i}^{\mathrm{AX\text{-}C}}$ are the VB energies of the pure and defected phases at the BZ point i, respectively.

The VBM alignment of AX-C and BX-D is obtained by combining the VBM alignment between the pure compounds BX/AX with the alignment between the alloyed phases AX-C/AX and BX-D/BX. The VBM alignment of BX/AX is given by

$$\Delta\varepsilon_{\mathrm{VBM}}^{\mathrm{BX/AX}} = \tilde{\varepsilon}_{\mathrm{VBM}}^{\mathrm{BX}} - \tilde{\varepsilon}_{\mathrm{VBM}}^{\mathrm{AX}}, \tag{9}$$

where $\tilde{\varepsilon}_{\mathrm{VBM}}^{i}$ is the energy of the VBM of compound i relative to the universal H +/- transition level. The change in the VBM of AX-C relative to AX can be calculated using an electrostatic alignment correction, $\Delta V_{\mathrm{PA}}^{\mathrm{AX\text{-}C}}$ following Ref. 48. Using this correction, we put the VBM of the AX-C supercell on the same energy scale as the VBM of the pure AX phase using

$$\Delta\varepsilon_{\mathrm{VBM}}^{\mathrm{AX\text{-}C/AX}} = \varepsilon_{\mathrm{VBM}}^{\mathrm{AX\text{-}C}} - \varepsilon_{\mathrm{VBM}}^{\mathrm{AX}} - \Delta V_{\mathrm{PA}}^{\mathrm{AX\text{-}C}}, \tag{10}$$

where $\varepsilon_{\mathrm{VBM}}^{i}$ is the VBM of system i (and similarly for BX-D). The VBM alignment of BX-D/AX-C is then

$$\Delta\varepsilon_{\mathrm{VBM}}^{\mathrm{BX\text{-}D/AX\text{-}C}} = \Delta\varepsilon_{\mathrm{VBM}}^{\mathrm{BX\text{-}D/BX}} - \Delta\varepsilon_{\mathrm{VBM}}^{\mathrm{AX\text{-}C/AX}} + \Delta\varepsilon_{\mathrm{VBM}}^{\mathrm{BX/AX}}. \tag{11}$$

Eqs. (8)–(11) hold for systems with AX matrix and AY nanostructure with no loss of generality.

TABLE II. Total 31 systems lie on the 4-D Pareto front of the descriptors.

Matrix AX	Nanostructure BX	Mat-Alloy C	Nano-Alloy D	Exp. System	ZT @ T (K)	Ref.
SnTe	CaTe	Pb	Se			
PbSe	SrSe	Ba	S			
PbTe	SrTe	Sn	Ba	PbTe–2% SrTe–1% Na_2Te	1.7 @ 815	23
				PbTe–4% SrTe–2% Na	2.2 @ 915	27
PbTe	SnTe	Ca	Ge			
PbTe	SnTe	Sr	Ge			
PbSe	SnSe	Sr	Ge			
PbSe	SnSe	Ba	Ge			
PbS	SnS	Ba	Se			
PbS	PbSe	Ca	Te			
PbS	PbSe	Sr	Te			
PbS	PbSe	Ba	Te			
PbSe	CaSe	Ba	S			
SnTe	SrTe	Pb	Ba			
PbSe	PbTe	Ba	Sn			
GeTe	GeSe	Sn	S			
GeTe	CaTe	Sn	Pb			
PbSe	CdSe	Sr	Ca	$Pb_{0.98}Na_{0.02}Se$–3% CdSe	1.4 @ 900	29
PbSe	CdSe	Ba	Ca			
PbSe	CdSe	Te	Ca			
PbTe	BaTe	Ca	Se			
PbS	CdS	Ba	Mg	$Pb_{0.975}Na_{0.025}$–3% CdS	1.3 @ 900	26
PbTe	PbS	Sn	Sr	$PbTe_{0.7}S_{0.3}$–2.5% K	2.2 @ 923	32
PbSe	GeSe	Ba	Te			
PbS	PbTe	Sr	Sn	$PbS_{0.97}Te_{0.03}$–0.1% $PbCl_2$	0.8 @ 900	25
PbS	PbTe	Ba	Sn			
GeTe	GeS	Sn	Se			
SnTe	BaTe	Pb	Se			
PbSe	MgSe	Ba	Ge			
GeTe	SrTe	Sn	Pb			
PbS	ZnS	Ba	Mg	$Pb_{0.975}Na_{0.025}S$–3% ZnS	1.2 @ 900	26
GeTe	BaTe	Sn	Se			

ACKNOWLEDGEMENT

The authors acknowledge support by the U.S. Department of Energy, Office of Science, Office of Basic Energy Sciences under Award Number DE-SC0014520. We acknowledge the use of the supercomputing resource facilities (Quest) at Northwestern University.

[1] J. Greeley, T. F. Jaramillo, J. Bonde, I. B. Chorkendorff, and J. K. Nrskov, Nature Materials **5**, 909 (2006).
[2] A. Jain, G. Hautier, C. J. Moore, S. Ping Ong, C. C. Fischer, T. Mueller, K. A. Persson, and G. Ceder, Computational Materials Science **50**, 2295 (2011).
[3] J. E. Saal, S. Kirklin, M. Aykol, B. Meredig, and C. Wolverton, JOM **65**, 1501 (2013).
[4] S. Curtarolo, G. L. W. Hart, M. B. Nardelli, N. Mingo, S. Sanvito, and O. Levy, Nature Materials **12**, 191 (2013).
[5] B. Meredig, A. Agrawal, S. Kirklin, J. E. Saal, J. W. Doak, A. Thompson, K. Zhang, A. Choudhary, and C. Wolverton, Phys. Rev. B **89**, 094104 (2014).
[6] R. Gautier, X. Zhang, L. Hu, L. Yu, Y. Lin, T. O. L. Sunde, D. Chon, K. R. Poeppelmeier, and A. Zunger, Nature Chemistry **7**, 308 (2015).
[7] S. Kirklin, J. E. Saal, B. Meredig, A. Thompson, J. W. Doak, M. Aykol, S. Rhl, and C. Wolverton, Npj Computational Materials **1**, 15010 (2015).
[8] See https://www.whitehouse.gov/mgi.
[9] G. K. H. Madsen, Journal of the American Chemical Society **128**, 12140 (2006).
[10] M. W. Gaultois, T. D. Sparks, C. K. H. Borg, R. Seshadri, W. D. Bonificio, and D. R. Clarke, Chemistry of Materials **25**, 2911 (2013).

[11] J. Carrete, W. Li, N. Mingo, S. Wang, and S. Curtarolo, Phys. Rev. X **4**, 011019 (2014).
[12] J. Yan, P. Gorai, B. Ortiz, S. Miller, S. A. Barnett, T. Mason, V. Stevanovi, and E. S. Toberer, Energy Environ. Sci. **8**, 983 (2015).
[13] P. Gorai, P. Parilla, E. S. Toberer, and V. Stevanovi, Chemistry of Materials **27**, 6213 (2005).
[14] H. Zhu, G. Hautier, U. Aydemir, Z. M. Gibbs, G. Li, S. Bajaj, J.-H. Phls, D. Broberg, W. Chen, A. Jain, M. A. White, M. Asta, G. J. Snyder, K. Persson, and G. Ceder, J. Mater. Chem. C **3**, 10554 (2015).
[15] S. Hao, F. Shi, P. D. Dravid, M. D. Kanatzidis, and C. Wolverton, Chemistry of Materials **9**, 3218 (2016).
[16] S. Hao, L. Ward, Z. Luo, V. Ozolins, V. P. Dravid, M. G. Kanatzidis, and C. Wolverton, Chemistry of Materials **31**, 3018 (2019).
[17] F. J. DiSalvo, Science **285**, 703 (1999).
[18] L.-D. Zhao, V. P. Dravid, and M. G. Kanatzidis, Energy Environ. Sci. **7**, 251 (2014).
[19] J. Androulakis, C.-H. Lin, H.-J. Kong, C. Uher, C.-I. Wu, T. Hogan, B. A. Cook, T. Caillat, K. M. Paraskevopoulos, and M. G. Kanatzidis, Journal of the American Chemical Society **129**, 9780 (2007).
[20] J. He, S. N. Girard, M. G. Kanatzidis, and V. P. Dravid, Advanced Functional Materials **20**, 764 (2010).
[21] S. N. Girard, J. He, C. Li, S. Moses, G. Wang, C. Uher, V. P. Dravid, and M. G. Kanatzidis, Nano Letters **10**, 2825 (2010).
[22] S. N. Girard, J. He, X. Zhou, D. Shoemaker, C. M. Jaworski, C. Uher, V. P. Dravid, J. P. Heremans, and M. G. Kanatzidis, Journal of the American Chemical Society **133**, 16588 (2011).
[23] K. Biswas, J. He, Q. Zhang, G. Wang, C. Uher, V. P. Dravid, and M. G. Kanatzidis, Nature Chemistry **3**, 160 (2011).
[24] K. Biswas, J. He, G. Wang, S.-H. Lo, C. Uher, V. P. Dravid, and M. G. Kanatzidis, Energy Environ. Sci. **4**, 4675 (2011).
[25] S. Johnsen, J. He, J. Androulakis, V. P. Dravid, I. Todorov, D. Y. Chung, and M. G. Kanatzidis, Journal of the American Chemical Society **133**, 3460 (2011).
[26] L.-D. Zhao, J. He, S. Hao, C.-I. Wu, T. P. Hogan, C. Wolverton, V. P. Dravid, and M. G. Kanatzidis, Journal of the American Chemical Society **134**, 16327 (2012).
[27] K. Biswas, J. He, I. D. Blum, C.-I. Wu, T. P. Hogan, D. N. Seidman, V. P. Dravid, and M. G. Kanatzidis, Nature **489**, 414 (2012).
[28] K. Ahn, K. Biswas, J. He, I. Chung, V. Dravid, and M. G. Kanatzidis, Energy Environ. Sci. **6**, 1529 (2013).
[29] L.-D. Zhao, S. Hao, S.-H. Lo, C.-I. Wu, X. Zhou, Y. Lee, H. Li, K. Biswas, T. P. Hogan, C. Uher, C. Wolverton, V. P. Dravid, and M. G. Kanatzidis, Journal of the American Chemical Society **135**, 7364 (2013).
[30] L. D. Zhao, H. J. Wu, S. Q. Hao, C. I. Wu, X. Y. Zhou, K. Biswas, J. Q. He, T. P. Hogan, C. Uher, C. Wolverton, V. P. Dravid, and M. G. Kanatzidis, Energy Environ. Sci. **6**, 3346 (2013).
[31] S. Hao, V. P. Dravid, M. G. Kanatzidis, and C. Wolverton, APL Materials **4**, 104505 (2016).
[32] H. J. Wu, L.-D. Zhao, F. S. Zheng, D. Wu, Y. L. Pei, X. Tong, M. G. Kanatzidis, and J. Q. He, Nature Communications **5**, 4515 (2014).
[33] G. Tan, S. Hao, J. Zhao, C. Wolverton, and M. G. Kanatzidis, Journal of the American Chemical Society **139**, 6764 (2017).
[34] Z.-Z. Luo, S. Hao, X. Zhang, X. Hua, S. Cai, G. Tan, T. P. Bailey, R. Ma, C. Uher, C. Wolverton, P. V. Dravid, Q. Yan, and M. G. Kanatzidis, Energy & Environmental Science **11**, 3220 (2018).
[35] S. Hao, P. D. Dravid, M. G. Kanatzidis, and C. Wolverton, npj Computational Materials **5**, 58 (2019).
[36] C. G. Van de Walle and J. Neugebauer, Nature **423**, 626 (2003).
[37] P. Godfrey, R. Shipley, and J. Gryz, The VLDB Journal **16**, 5 (2007).
[38] V. Pihur, S. Datta, and S. Datta, BMC Bioinformatics **10**, 62 (2009).
[39] T. Bligaard, G. H. Jhannesson, A. V. Ruban, H. L. Skriver, K. W. Jacobsen, and J. K. Nrskov, Applied Physics Letters **83**, 4527 (2003).
[40] K. Lejaeghere, S. Cottenier, and V. Van Speybroeck, Phys. Rev. Lett. **111**, 075501 (2013).
[41] J. W. Doak and C. Wolverton, Phys. Rev. B **86**, 144202 (2012).
[42] P. Hohenberg and W. Kohn, Phys. Rev. **136**, B864 (1964).
[43] W. Kohn and L. J. Sham, Phys. Rev. **140**, A1133 (1965).
[44] G. Kresse and J. Furthmller, Phys. Rev. B **54**, 11169 (1996).
[45] J. P. Perdew, K. Burke, and M. Ernzerhof, Phys. Rev. Lett. **77**, 3865 (1996).
[46] P. E. Blchl, Phys. Rev. B **50**, 17953 (1994).
[47] C. Spearman, Br. J. Psychiatry **2**, 89 (1906).
[48] S. Lany and A. Zunger, Phys. Rev. B **78**, 235104 (2008).